NUMERICAL SIMULATION OF CLOUD DROP IMPINGEMENT ON A HELICOPTER

Krzysztof Szilder*, Edward Lozowski**
***Institute for Aerospace Research, National Research Council, Ottawa, Canada,**
****Department of Earth & Atmospheric Sciences, University of Alberta, Edmonton, Canada**

Keywords: *supercooled drops, icing, rotorcraft aerodynamics, CFD*

Abstract

In this paper, we describe the results of a numerical model of the time-dependent trajectories and impingement of cloud drops on a Bell 412 helicopter in two configurations: 1. an isolated tail rotor and 2. a helicopter with rotating main rotor in forward flight. The unsteady flow field was obtained from the CFD-FASTRAN solver used with the Euler governing equations. Drops were inserted into the time-dependent, three-dimensional airflow and drop trajectories were computed using a Lagrangian approach. The characteristics of the drop trajectories and their impingement on the rotating blades and fuselage were examined. Whereas the maximum impingement rate for the rotors was observed in the vicinity of the leading edge, the intensity of impingement on the fuselage reached a maximum near its extremities. For the conditions described in the paper, the drop mass impingement rate on the isolated tail rotor is 0.6 kg/min, on the main rotor 3 kg/min, and on the fuselage 0.25 kg/min, with a cloud liquid water content of 0.5 g/m^3.

1 Introduction

Ice formation on the components of rotary-wing aircraft can often be hazardous. Ice deposits can degrade the aerodynamic performance of an aircraft due to a reduction in lift and an increase in drag. In addition, ice forming on helicopter rotor blades is particularly dangerous, because the rotor blades can become significantly unbalanced when ice is shed asymmetrically, leading to severe vibrations. Large pieces of shed ice can impact the aft airframe or tail rotor, with potentially dangerous consequences. Research into ice accretion on helicopters is fairly active. Some recent experimental results are described in [1], while numerical investigations may be found in [2, 3].

The work discussed in this paper is a component of NRC's predictive capabilities development for ice formation on a helicopter. Data on drop impingement on the rotor blades and fuselage, together with airflow and heat transfer conditions, are necessary inputs to NRC's unique ice accretion model. This icing model is based on a discrete particle approach with the ability to predict the shape, structural details and physical properties of ice accretions, by emulating the behaviour of individual fluid elements. It has been shown that this approach can be successfully applied to the simulation of in-flight icing [4]. Some recent, preliminary research has shown that the model can be used to predict ice accretion on a helicopter fuselage in a simplified configuration without a rotor [5]. Our early work on the simulation of drop impingement on an isolated main rotor in hover is described in [6].

The objective of the research described in this paper is to develop a predictive capability for drop impingement on helicopter rotor blades and the fuselage. This task consists of two parts: 1. solving the governing equations describing the airflow with a rotating rotor, and 2. developing an algorithm to predict drop trajectories and their impingement. The first step has been described in [7]; only a brief outline is given in the next section. The focus of the paper is on the examination of drop trajectories and their impingement pattern and intensity. Numerical analysis of drop impingement on an isolated tail rotor is of

particular interest, since we plan to validate the numerical results with full-scale wind tunnel icing tests of the Bell 412 tail rotor.

2 Three-Dimensional Numerical Model

The flight aerodynamics of rotary-wing aircraft presents a great challenge since it involves a variety of complex flow phenomena. In addition to modelling the complicated flow physics, the unique problem of grid generation has to be resolved. These issues have been addressed over time as discussed in [8]. In our drop trajectory computations, we employ the results of two CFD studies of unsteady flow past a Bell 412 helicopter: 1. an isolated two-bladed tail rotor; and 2. the four-bladed main rotor with the fuselage in forward flight conditions. The unsteady flow fields were computed using the CFD-FASTRAN solver [9], with the Euler equations used as the governing equations. This simplification significantly alleviates the grid density requirement near structural surfaces and therefore greatly reduces the CPU time and memory requirements for the simulation. The Chimera moving grid technique was applied to represent the blade motion.

The time-dependent, three-dimensional flow field, which was the output of the flow field solver, was used as input to our drop trajectory solver. The airflow solver provided values of the Cartesian velocity components, discretized in space and time. However, in order to compute drop trajectories, values of flow velocity are required at drop locations, which lie typically between the discrete time frames of 3D grid points. To overcome the spatial discretization issue, the velocity components at the location of the drop were computed as a weighted average of the values at the eight grid points surrounding the point where the drop velocity was needed. An inverse distance weighting scheme was used. To resolve the time discretization problem, linear interpolation between two neighbouring, discrete time frames was used to compute the velocity at a specific intermediary time.

Cloud drops were inserted into the time-dependent airflow with an initial velocity equal to that of the airstream and drop trajectories were computed using a Lagrangian approach. It was assumed that the cloud drops were spherical and that they did not perturb the airflow. Two forces were considered to act on the drops: the aerodynamic drag arising from their motion relative to the airstream and the gravitational force. The equation of drop motion used in the model is similar to that used in other icing-related models [10]. In order to solve the Lagrangian equation of drop motion, a fourth-order Runge-Kutta method was implemented. The trajectory step size was taken to be 0.01 m away from the rotor and fuselage, but for enhanced impingement precision, the step size was decreased to 0.002 m close to impingement. The time step was determined by the trajectory step and local drop speed.

In the isolated tail rotor case, the following parameter values were assumed: free stream air speed 15.4 m/s in a direction perpendicular to the rotor axis, drop diameters 20 and 50 μm, rotor speed 1660 rpm, and blade pitch angle 9 degrees. The time frame interval, used for the trajectory calculations and obtained from the flow solver, was every 5 degrees of blade rotation (approximately 0.5 ms).

In the computations of airflow around the helicopter in forward flight, the tail rotor was not included. The main rotor blade cross-section profiles were twisted in the span-wise direction and the blade chord was tapered near the tip. The following parameters were assumed: helicopter forward flight speed 9.7 m/s, drop diameter 50 μm, rotor speed 324 rpm, blade coning angle 12.3 degrees, blade pitch angle varied harmonically, and the time frame interval every 15 degrees of blade rotation (approximately 7.7 ms).

3 Model Results and Discussion

In this section, we examine the trajectories of cloud drops in the isolated tail rotor configuration and subsequently in the helicopter forward flight configuration. Of particular interest are drops that impinge on the rotor blades and on the fuselage.

3.1 Tail Rotor

Initially, the supercooled drops are located upstream of the tail rotor, on a y-z plane parallel to the tail rotor rotation axis; the distance between the axis of rotation and this plane is 5 m, Figure 1. Numerical testing showed that locating the initial plane at a greater distance does not alter the overall results. The initial drop velocity was set equal to the local airflow velocity. In order to visualize the overall drop trajectory pattern, three families of trajectories, initially separated by a vertical distance of 1 m and with an initial horizontal spacing of 0.1 m are shown in Figure 1. Drops of 20 μm and 50 μm diameters are input at the same locations at the same time. It is apparent that the trajectories are pushed sideways in a swirling motion by the airflow generated by the rotating tail rotor. Due to their greater inertia, the larger drops respond more slowly to the changing airflow field. As a result, the trajectories tend to have smaller curvature.

Because of the periodic motion of the two-bladed tail rotor, the airflow is periodic with a period of one-half the rotor revolution period (approximately 18.1 ms). Since the flow field is time-dependent, the drop trajectories are also time-dependent. In order to illustrate some of the drop trajectory time variability, two cases, t_1 and t_2, were examined. The two cases differ in drop release times by half the airflow period (approximately 9.0 ms).

In order to examine the drop impingement intensity and its pattern on the tail rotor blades, 50 μm drops were initially positioned upstream on a square grid, with a spacing of 0.01m. The left part of Figure 2 shows the initial positions of only the impinging drops. The initial locations of impinging drops are depicted by red dots for time t_1, and blue dots for time t_2. The locations of impinging drops on the initial plane clearly depend on the drop release time. However, it appears that the initial positions of all impinging drops lie within the envelope shown in Figure 2. We estimate that approximately 14% of all possible trajectories that start from inside this initial envelope actually impinge on the tail rotor. Drop impingement locations on the tail rotor in non-rotating and rotating frames of reference are shown on the right hand side of Figure 2.

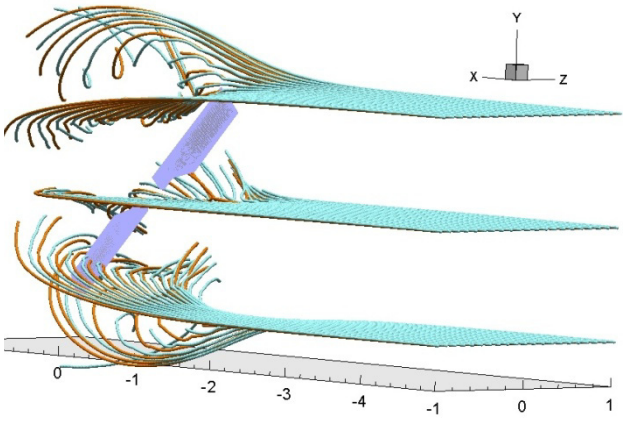

Fig. 1. Drop trajectories for the isolated tail rotor configuration, with drop diameters 20 μm (cyan) and 50 μm (orange). The spatial scale is in metres.

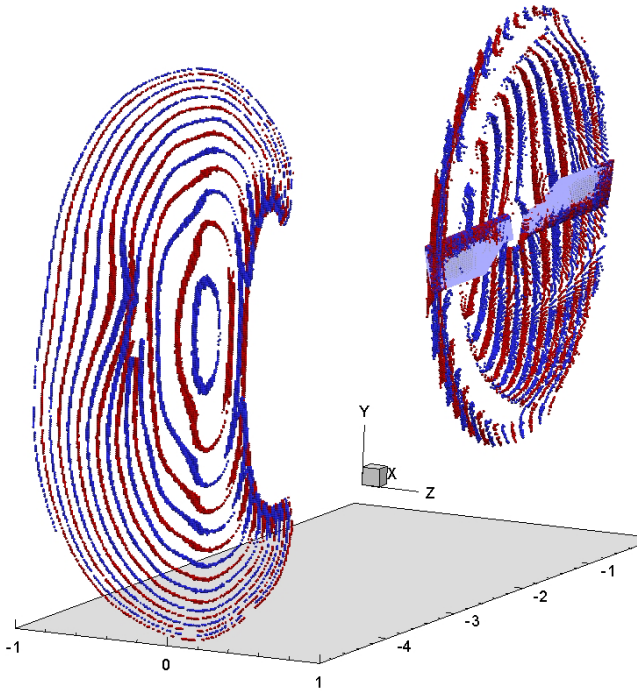

Fig. 2. Insertion locations (left) and impact locations (right) of 50 μm drops. The spatial scale is in metres.

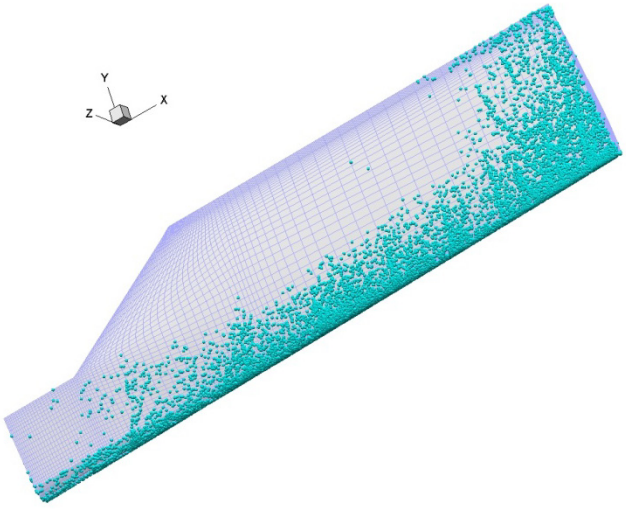

Fig. 3a. Drop impingement locations on the suction surface of a tail rotor blade. For image clarity, drop size is exaggerated.

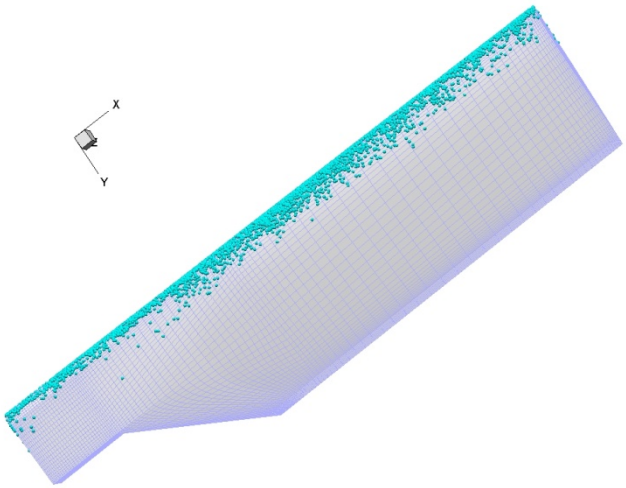

Fig. 3b. Drop impingement locations on the pressure surface of a tail rotor blade.

The impingement points of the drops on the two tail rotor blades are superimposed onto one blade and shown in Figure 3. Times t_1 and t_2 have also been combined in this figure. It is evident that the intensity of drop impingement is greatest close to the leading edge, on both the suction and pressure surfaces. There is also substantial impingement on the aft portions of the suction surface close to the blade tip. Impingement occurs only close to the leading edge on the pressure surface.

The number of impinging drops can be used to estimate the distribution of the impinging mass flux on the tail rotor. Assuming that each impinging trajectory is representative of the entire initial 0.01 m grid square surrounding it, the impinging mass rate may be estimated knowing the number of impinging trajectories, the free stream velocity and the liquid water content. In devising Figure 4, the average impinging trajectory numbers for times t_1 and t_2 were used.

Figure 4a shows the radial distribution of the impinging drop mass flux on one of the tail rotor blades, averaged over 0.1 m blade sectors and displayed as a function of the distance from the axis of rotation. In addition to the total impinging mass flux, the impinging mass flux in the vicinity of the leading edge is also shown. The vicinity of the leading edge is defined here as the blade surface within 0.02 m of the leading edge, measured along the chord. The distribution of the total impinging mass flux on the rotor has a local maximum around 0.8 m from the axis of rotation (while this fact is not immediately apparent from Figure 3, closer analysis reveals higher density of impingement there); beyond that it initially decreases then reaches a maximum close to the rotor tip. The impingement flux in the leading edge vicinity exhibits a similar radial variation, but its magnitude is smaller, particularly near the blade tip. This is related to the extensive drop impingement on the entire suction rotor surface within 0.2 m from the rotor tip.

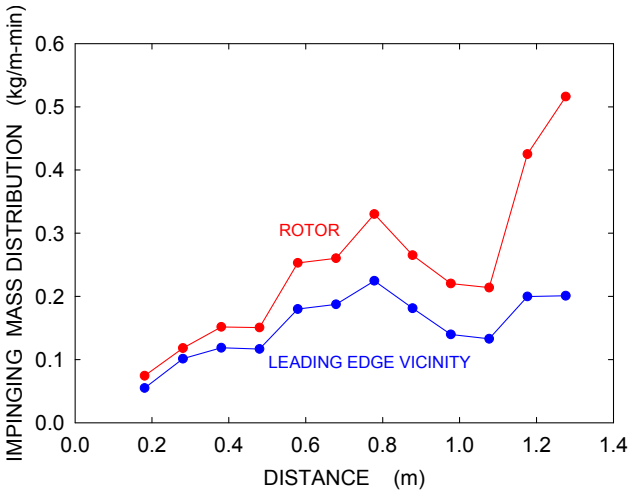

Fig. 4a. Radial distribution of impinging mass flux on a tail rotor blade. Drop size 50 µm and liquid water content 0.5 g/m^3.

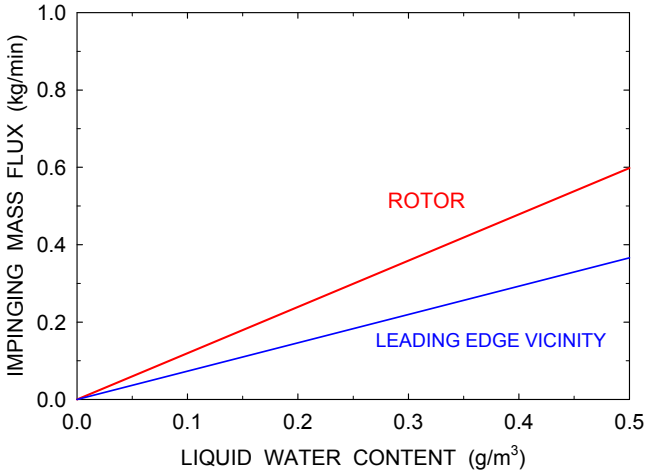

Fig. 4b. Total impinging mass flux on the tail rotor. Drop size 50 μm.

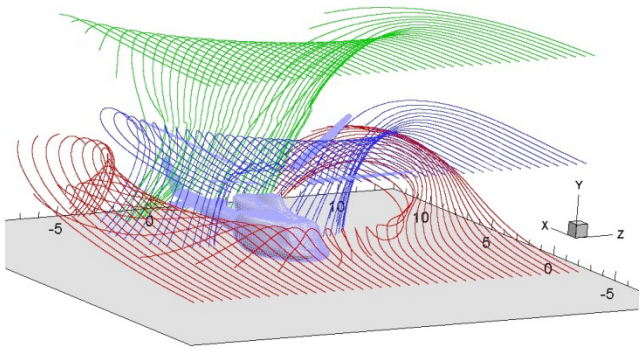

Fig. 5. Drop trajectories in helicopter forward flight conditions. The spatial scale is in metres.

Integration of the distribution of the drop impingement mass flux along the blade span gives the impingement for the entire tail rotor. The rate of mass impingement for the entire tail rotor and for the leading edge vicinity, for both blades combined, is shown as a function of liquid water content in Figure 4b. Approximately 60% of total impingement occurs in the vicinity of the leading edge. The rate of mass impingement is linearly proportional to the liquid water content. For LWC of 0.5 g/m^3, the predicted rate of mass impingement for the tail rotor is 0.60 kg/min, while the leading edge region experiences a mass impingement rate of 0.36 kg/min.

3.2 Helicopter Forward Flight

A similar analysis was performed for a helicopter in forward flight. For this case, the drops are introduced upstream of the helicopter, on a y-z plane perpendicular to the helicopter's plane of symmetry; the distance between this plane and the fuselage nose is 9.75 m, Figure 5. Three families of trajectories initially separated by a vertical distance of 5 m and with an initial horizontal spacing of 0.5 m are shown in Figure 5. On approach to the helicopter, the trajectories swirl downward, as they are carried along by the airflow generated by the moving main rotor blades.

In order to examine drop impingement on the helicopter rotor blades and fuselage, drops were introduced upstream on a square grid with a spacing of 0.05 m. In order to illustrate the temporal variability of the drop trajectories, two drop release times, t_1 and t_2, were considered. The two cases differ in drop release time by half the airflow period (one-eighth of the revolution period or approximately 23.1 ms). Figure 6a shows the initial positions of only the impinging drops. Drop insertion locations corresponding to rotor impingement are depicted by red dots for time t_1, and by blue dots for time t_2. Drop insertion locations that lead to fuselage impingement are depicted by dark green dots for both cases. We estimate that approximately 6% of all possible trajectories, starting inside the insertion envelope shown in Figure 6a, actually impinge on the helicopter's rotor and fuselage. The impingement points of the drops are shown in Figure 6b in a non-rotating frame of reference. Approximately 92% of the impingement occurs on the main rotor and 8% on the fuselage. There is a considerable drop impingement on the tail boom and horizontal stabilizer.

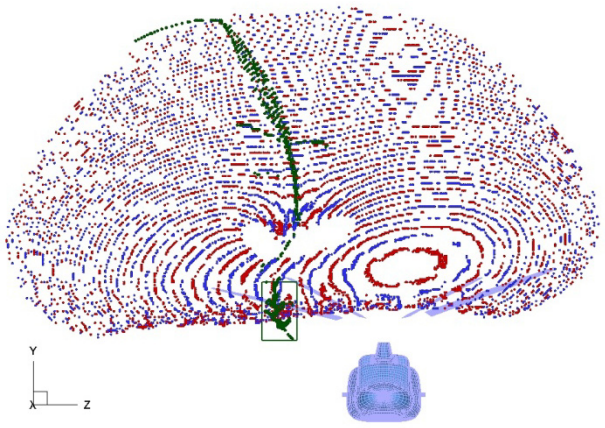

Fig. 6a. Insertion locations of drops impinging on the rotor (red and blue) and on the fuselage (dark green). The insertion plane is 7.5m ahead of the fuselage nose.

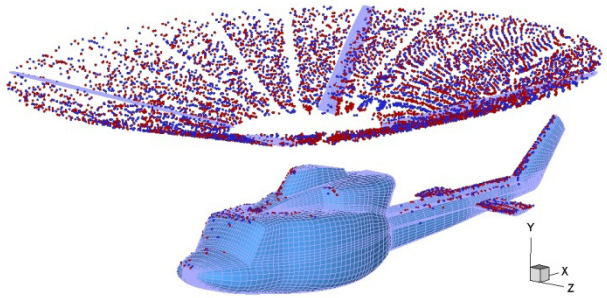

Fig. 6b. Drop impingement locations on the main rotor (non-rotating frame of reference) and fuselage.

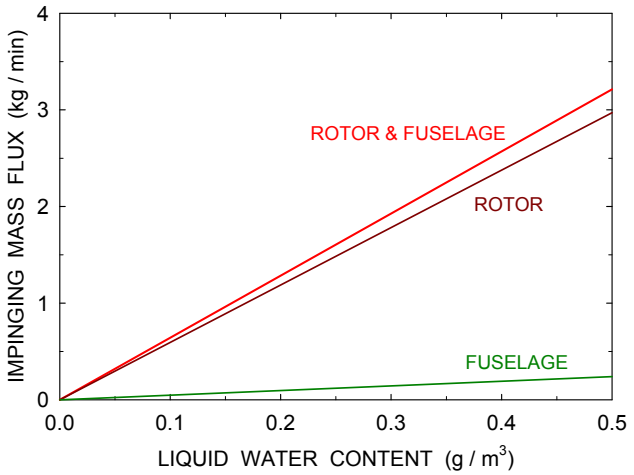

Fig. 7. Impinging mass flux on the main rotor and fuselage.

The total number of impinging trajectories can be used to estimate the impinging mass flux on the main rotor and fuselage. Assuming that each trajectory is representative of the entire initial 0.05 m grid square surrounding it, the impinging mass flux may be computed knowing the number of impinging trajectories, the helicopter forward speed and the liquid water content. Impingement mass is linearly proportional to the liquid water content, Figure 7. For a LWC of 0.5 g/m^3, the predicted impinging mass flux for all blades of the main rotor combined is 3.0 kg/min, while the fuselage receives 0.25 kg/min.

In order to examine drop impingement on the fuselage in greater detail, a finer grid of drop insertion locations was used, Figure 8. Drops were placed on a square grid with a spacing of 0.02 m, within a rectangle of 1.2 m by 2.0 m, depicted by the green outline. In order to reduce the computational effort of the analysis, it was assumed that the drops are not intercepted by the rotor. Accounting for rotor sweep out would remove around 92% of the drops but would not significantly affect the distribution over the fuselage. The dark green dots in Figure 8 depict the initial and final points of impinging trajectories, while the green colour depicts the trajectories themselves. It is apparent that the drops tend to impinge on the fuselage extremities as the trajectories diverge from the streamlines. In addition, the rotor swirl induces an asymmetry in the impingement pattern with a higher flux on the starboard side of the aircraft.

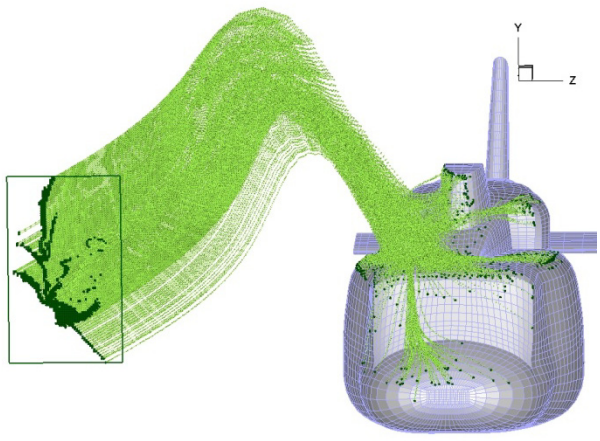

Fig. 8. Trajectories of drops impinging on the fuselage.

4 Conclusions

In this paper, we have demonstrated that it is feasible, with reasonable computational effort, to predict time-dependent, cloud drop impingement on Bell 412 helicopter rotors and fuselage. The analysis for an isolated tail rotor indicates that approximately 60% of the total mass flux impinges in the vicinity of the leading edge. The impingement intensity reaches a maximum close to the rotor tip. For a cloud liquid water content of 0.5 g/m^3, the predicted total impinging mass flux for the isolated tail rotor is 0.6 kg/min. Analysis of the helicopter in forward flight indicates that 92% of impingement occurs on the rotor blades and 8% on the fuselage under the examined conditions. For a cloud liquid water content of 0.5 g/m^3, the predicted impinging water mass flux on main rotor blades is 3.0 kg/min and on the fuselage 0.25 kg/min. Analysis of the drop impingement pattern on the fuselage suggests that the maximum impingement occurs near the fuselage extremities.

In the near future, we will be performing icing wind tunnel experiments to validate the model. We plan to mount a full-size Bell 412 tail rotor in the NRC Propulsion and Icing Wind Tunnel and expose it to a supercooled cloud drop environment. We also plan to combine drop impingement with flow and heat transfer computations in order to predict ice formation on the tail rotor. Subsequent research will focus on ice shedding and the potential impact of shed ice on aircraft safety.

Acknowledgement

The authors wish to thank Mr. Steve Zhang, Institute for Aerospace Research, National Research Council, Canada, for sharing the results of his numerical simulation of airflow past a Bell 412 helicopter.

References

[1] Flemming R J and Alldridge P J. Sikorsky S-92A and S-76D helicopter rotor ice protection systems. *SAE Aircraft & Engine Icing International Conference*, Seville, Spain, 2007-01-3299, 2007.

[2] Zanazzi G, Mingione G, Pagano A, Visingardi A and Narducci R. Ice accretion prediction on helicopter rotor blade in hover flight. *SAE Aircraft & Engine Icing International Conference*, Seville, Spain, 2007-01-3309, 2007.

[3] Aube M S, Baruzzi G S, Habashi W G and Aliaga C N. Application of FENSAP-ICE-Unsteady to helicopter icing. *SAE Aircraft & Engine Icing International Conference*, Seville, Spain, 2007-01-3310, 2007.

[4] Szilder K and Lozowski E P. Novel two-dimensional modeling approach for aircraft icing. *Journal of Aircraft*, Vol. 41, No. 4, pp. 854-861, 2004.

[5] Szilder K. Numerical simulation of ice formation on a helicopter fuselage. *SAE Aircraft & Engine Icing International Conference*, Seville, Spain, 2007-01-3308, 2007.

[6] Szilder K and Xu H. Prediction of supercooled droplet impingement on helicopter rotor blades. ICAS 2008, *26th International Congress of the Aeronautical Sciences*, Anchorage, USA, ICAS 2008-2.6.4, 2008.

[7] Zhang F, Xu H, Ball N G and Gubbels A W. Numerical flow simulations past a Bell 412 helicopter in real-time hover, low and high forward speed flight conditions using Chimera grid technique. *34th European Rotorcraft Forum*, Liverpool, UK, 2008.

[8] Strawn R C, Caradonna F X and Duque E P N. 30 years of rotorcraft Computational Fluid Dynamics research and development. *Journal of the American Helicopter Society*, pp. 5-21, January 2006.

[9] CFD-FASTRAN Software Manual, CFD Research Corporation, Huntsville, AL, 2002.

[10] Kind R J, Potapczuk M G, Feo A, Golia C and Shah A D. Experimental and computational simulation of in-flight icing phenomena. *Progress in Aerospace Sciences*, Vol. 34, Issues 5-6, pp. 257-345, 1998.

Copyright Statement